Origin of cell contrast in offset aperture adaptive optics ophthalmoscopy

A. Guevara-Torres,[1,2,*] ⓘ **D. R. Williams,**[1,2] AND **J. B. Schallek**[1,3,4]

[1]Center for Visual Science, University of Rochester, Rochester, New York 14642, USA
[2]The Institute of Optics, University of Rochester, Rochester, New York 14620, USA
[3]Flaum Eye Institute, University of Rochester, Rochester, New York 14642, USA
[4]Department of Neuroscience, University of Rochester, Rochester, New York 14620, USA
*Corresponding author: rguevara@optics.rochester.edu

Offset aperture and split detector imaging are variants of adaptive optics scanning ophthalmoscopy recently introduced to improve the image contrast of retinal cells. Unlike conventional confocal scanning ophthalmoscopy, these approaches collect light laterally decentered from the optical axis. A complete explanation of how these methods enhance contrast has not been described. Here, we provide an optical model with supporting *in vivo* data that show contrast is generated from spatial variations in the refractive index as it is in phase contrast microscopy. A prediction of this model is supported by experimental data that show contrast is optimized when the detector is placed conjugate with a deeper backscattering screen such as the retinal pigment epithelium and choroid, rather than with the layer being imaged as in conventional confocal imaging. This detection strategy provides a substantial improvement in the contrast these new methods can produce.   © 2020 Optical Society of America

Offset aperture and split detection are techniques recently introduced in ophthalmoscopy that have increased the image contrast of translucent retinal structures [1–7]. While the exact implementation varies, these methods have in common the fact that they detect light that is displaced laterally from the on-axis location where the detection pinhole is positioned in a conventional confocal microscope. Combined with adaptive optics that measure and correct for aberrations of the eye, these non-confocal methods can directly image red blood cells, horizontal cells, ganglion cells, as well as photoreceptor inner segments and somas without the need for contrast agents [1–7]. Examples of split detection images obtained in the living mouse retina are shown in Fig. 1.

Despite the utility of rendering translucent cells visible, explanations for the mechanism that provides cellular contrast with these approaches are incomplete. Elsner and Chui attribute the optical contrast to multiply scattered light [1,6]. In this model, illumination light that strikes the target object is scattered onto deeper retinal layers that then backscatter the light

onto the detector. This model, which they attribute to forward and multiple scatter, is supported by evidence of improved contrast of blood vessels where they pass over the margin of the more highly reflective margin of the optic disc [1]. Here we build upon their model to explain a yet unaccounted for feature of such images: the asymmetric appearance of cells where one edge of the cell looks bright and the opposite edge appears dark. This is very similar to the appearance of differential interference contrast (DIC) [8] images, which begs the question as to whether offset aperture and split detection imaging are actually variants within the family of phase contrast methods.

In this Letter, we show how these methods convert refractive index gradients into intensity variations across cellular features in the image. We propose that, as the scanning beam encounters refractive index gradients within and between single cells, these gradients, depending on their size and sign, steer the beam in different directions and by different amounts away from the optical axis. When these deviated beams arrive at a deeper backscattering layer, they create decentered light distributions that when sampled by the detector pinhole, create the asymmetric light distributions that produce the contrast in single cells. Figure 2 shows our model based on the mouse eye that captures this concept. Figure 2(a) explains the essential principle using simple geometric optics. In Fig. 2(a), we assume that each cell body has a higher refractive index than the surrounding tissue, so that it acts as a weak positive lens (the negative lens condition is discussed later). Light passing through opposite sides of the cell body will be steered in opposite directions away from the optic axis. Consistent with the model of Chui and Burns [1], we assume that this redirected light propagates to a backscattering layer deeper in the retina, creating an intensity distribution on this screen that captures the deviation of the beam as it is scanned across the cell body. If the detection pinhole is offset from the optical axis, the deviations in the beam will result in either an increase or a decrease in the intensity, depending on whether the cellular lensing has deviated the beam at each scanning location toward or away from a decentered detector.

To generate quantitative predictions about the asymmetry expected from geometrical optics, we also developed a wave optics model. We modeled the soma of a single photoreceptor
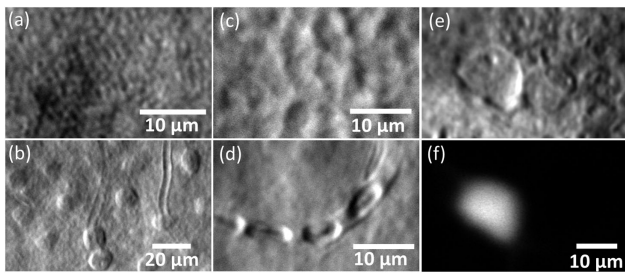
Fig. 1. Retinal structures captured with split detection in the living mouse eye. (a) Photoreceptor distal processes. (b) Horizontal cells. (c) Photoreceptor somas. (d) Red blood cells. (e) Ganglion cell identified by simultaneously captured Thy-1 YFP fluorescence [9,10] shown in (f) and axonal imaging. Images (a)–(d) adapted from [3,4].

as a 5 μm sphere with a uniform refractive index corresponding to the mean refractive index of 1.4 taken from [11] immersed in a lower refractive index medium, assumed to be 1.36 [11]. We modeled the illumination to be an Airy pattern. Pattern phase but not amplitude was modified by a 2D matrix of complex numbers. The absolute value of these complex numbers is one. The phase is the optical path length (in waves) calculated along the direction of propagation of a 3D model of the cell. The illumination point spread function (PSF) is 1.9 μm in diameter and is calculated by the Fourier transform of the pupil function [12] estimated from a pupil of the eye of 2 mm in diameter, an eye focal length of 2.6 mm [13], and a light source of 796 nm. The light continues forward using Fraunhofer propagation [12] towards a deeper screen.

The return path of light was modeled as the intensity light distribution at the deeper screen convolved with a geometrical PSF (a disk of uniform intensity). The return PSF was determined by the NA angle of the eye and the defocus distance between the screen and the virtual position of the detector. The geometrical PSF was used because defocus range across layers in the retina is large (60 diopters) [12]. Based on optical coherence tomography (OCT) evidence captured with a Spectralis HRA + OCT (Heidelberg Engineering, spectrum centered at 870 nm), we assumed that the cell lay 100 μm in front of a backscattering layer corresponding in the mouse to a layer approximately 30 μm thick, which corresponds to the retinal pigment epithelium (RPE) and choroid [14]. The thick layer was simulated as five discrete retinal reflective layers. At the detection plane, the simulations for each of the five discrete layers were averaged as intensities [15], and then we considered an offset detector with the characteristics of the pinhole we used in the experiments. Finally, this process was repeated for multiple scan positions.

Figure 2(b) shows the calculated light distribution at the backscattering layer when the left and right sides of the cell are illuminated. The areas in red show the light intensity detected in each case. Figure 2(c) shows the calculated intensity distribution as the beam is scanned across the entire cell, which captures qualitatively the asymmetry observed in offset aperture imaging.

An unexpected prediction of this model shown in Fig. 2(d) is that the maximum contrast of this asymmetry should occur when the detector is conjugate with a plane amid the backscattering layers rather than the layer conjugate to the object; the convention in current split detection and offset aperture imaging. If the detector is positioned axially either in front of or behind the backscattering layer, it will capture light from a
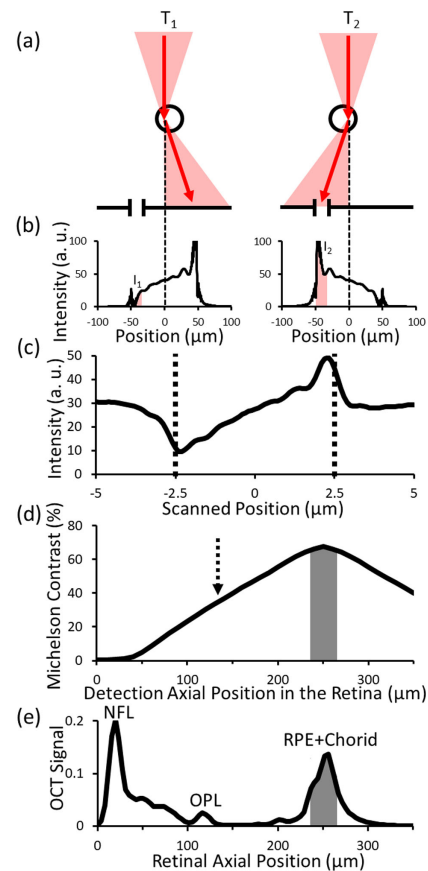
Fig. 2. Wave optics model of offset aperture. (a) Geometrical model for offset aperture. When the beam is focused into the edge of a cell, the beam will be deviated into a direction that can match the detector offset detector. (b) Wave optics model of the light distribution at the detection plane is deviated to either the right or the left as the beam is scanned across the cell. (c) Simulated lens profile of a spherical cell as detected with a simulated offset aperture detector with a 20 Airy disc diameter (ADD) displacement and a pinhole diameter of 8.6 ADD. The vertical lines show the boundary of the cell. (d) By simulating the effect of the detector displacement, we find that the optimum detection plane is when the detector is conjugate to the deeper reflective thick layer. We find that with axial displacement, the contrast increases by a factor of 1.8. The arrow shows the axial location of the illuminated cell. The shaded area shows the location of the thick backscattering layer. (e) Retinal OCT profile captured in the living mouse eye.

defocused image of the light distribution illustrated in Fig. 2(b). This will inevitably blur the intensity variations that convey the phase variations in the original plane to be imaged.

To test the model prediction, we used an adaptive optics scanning light ophthalmoscope (AOSLO) designed specifically to image the mouse retina [9]. In brief, we used a 904 nm (8 μW) laser for wavefront sensing and 796 nm light with 17 nm bandwidth (480 μW, Superlum, Ireland) for imaging. A membrane based deformable mirror (ALPAO, France) provided aberration correction. This scanning instrument has a frame rate of 25 Hz. To correct for small residual motion within the mouse eye, a second 640 nm visible laser (30 μW, Toptica, Germany) was used to simultaneously image the retina in confocal mode using a separate, visible light photomultiplier tube (PMT). This provided simultaneous, dual-channel image registration

without impacting the measurements performed in the near infrared [16].

We imaged two classes of retinal structures because they provide strong contrast in the offset and split detection configurations [3,4] and lie at different distances from the deeper backscattering layer hypothesized to be key to capturing the refracted light.

The diameter of the detector aperture was 200 μm (equal to 8.6 Airy disc diameter (ADD)). Similar to the offset aperture approaches of Sulai, Chui, Rossi, and Guevara [1,3,5,7], we displaced the detector pinhole laterally in the *en face* plane. We chose displacements of 10 ADD for vessels, and 22 and 35 ADD for experiments imaging horizontal cells. These values were kept constant throughout the experiment.

With the axial position of the illumination kept focused on the retinal structure of interest, we collected images at each of a number of axial locations of the detector by sliding the PMT together with a circular pinhole in the axial dimension. Maxwell's elongation formula provided the relationship between an axial displacement of the detector and its corresponding displacement at the retina [17]. For our system, an axial displacement of 1 mm at the detector corresponded to an axial displacement of 9.8 μm in the retina. The detector was translated by up to 215 μm (38 diopters) in retinal distance from the position where it was conjugate with the illumination plane, as is the case in conventional confocal imaging.

Figure 3 shows the contrast improvement realized from the axial displacement of the detector toward a deeper plane for both horizontal cells and capillaries. The Michelson contrast of the light and dark asymmetry in horizontal cells was not highest when the detector was conjugate with the illumination plane. Yet consistent with the predictions of the model, the contrast increased to a local maximum with a detection 117 μm deeper, corresponding to the location of the backscattering screen consistent with OCT images. The contrast in the optimized detection plane was 1.9 times higher when calculating Michelson contrast in the average frame. The improvement in contrast was observed in all six cells across three mice (Fig. 3, black trace) and is anatomically consistent with the distance between horizontal cells and the photoreceptor/RPE boundary (102 μm [18]).

To test that this was not a special case, true for only one type of structure in the retina, we also tested the model prediction for capillaries. When imaging capillaries at the outer plexiform layer [OPL, Fig. 3(b) red data], we observed a broad contrast maximum at roughly the same axial location in the retina as was found for horizontal cells (Visualization 1). Though the contrast of capillaries was relatively lower, the contrast benefit of shifting the axial position of the detector to the backscattering plane was similar to that found for horizontal cells, about 1.9 times.

Given that capillaries reside in three discrete axial locations within the mouse retina [19], we repeated the experiment with capillaries at the ganglion cell layer (GCL), which are ∼100 μm vitread to those in the OPL. While limited *z*-stroke of the detector (25 mm) precluded measurements of local contrast maxima of GCL capillaries, the data followed a trend similar to that obtained at the OPL throughout the extent of overlap of the two data sets (Fig. 3, blue data). Differences in absolute contrast were less than those predicted, due likely to the scatter from the complex anatomy of the retina. Moreover, the contrast benefit
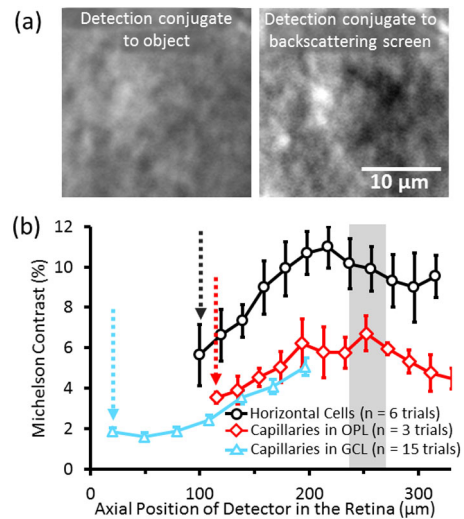

Fig. 3. Experimental data show an increase in the contrast by moving the detector towards a deeper reflective layer in agreement with simulations. (a) Increase in contrast of horizontal cells by axially displacing the detector from $z = 100$ μm (conjugate to the illuminated cell, left image) to $z = 237$ μm (right image). Horizontal cell images are normalized to the mean intensity and displayed with the same contrast range. (b) Horizontal cells (black curve) show a local maximum when the detector is displaced 117 μm in retinal coordinates. We observe a very similar behavior with capillaries in the OPL (red curve); they also show a maximum in the contrast at a layer coincident with the deeper backscattering layer. These data are also shown in Visualization 1. In the experiments with capillaries at the ganglion cell layer (blue curve), we observe an increase in the contrast in a direction consistent with where a deeper thicker reflective screen is expected to be. Blue curve does not show a maximum due to the limits of detector stroke in the axial dimension. Vertical arrows show the position of illumination focus for each condition. The shaded region corresponds to the thick backscattering layer [Fig. 2(e)]. Error bars represent standard error of the mean.

was at least 2.7-fold, similar to the 1.9× improvement of the OPL capillaries.

These results are consistent with the model proposed here and are counterintuitive in the context of conventional practice in confocal imaging in which the illumination and detection planes coincide. We found that retinal structures could be imaged with the highest contrast despite moving the detector plane as much as 38 diopters (215 μm in retinal distance) away from the illumination plane, which was $> 20\times$ larger than the axial resolution of (∼9 μm). If backscatter from the object was the sole source of image contrast, any target object 38 diopters away would be virtually unrecognizable due to blur. In the preferred configuration proposed here in which the illumination and detection planes are axially displaced, the illumination focus provides optical resolution and axial sectioning for the target object, while the detector displacement optimizes contrast.

For these experiments, there are several advantages to using the living mouse eye, which has a NA of 0.49 [13], twice that of the human, providing a two-fold increase in lateral resolution and a four-fold increase in axial resolution [9]. Lateral resolution is ∼700 nm, consistent with theoretical predictions [9]. The axial PSF is theoretically 9 μm [17], comparable to the size of many retinal cell bodies. In addition to providing resolution
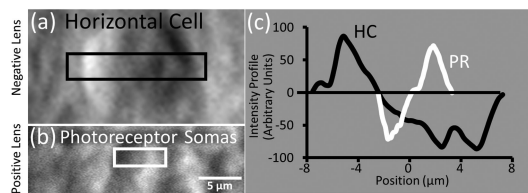
Fig. 4. Polarity change between (a) horizontal cell and (b) photoreceptor soma. (c) Intensity profile plot of the horizontal cell (HC) in (a) and the photoreceptor soma (PR) in (b).

superior to that of a human eye, the high NA of the mouse eye entails a narrower depth of field, increasing the sensitivity with which we can identify the focal plane optimizing image contrast. In addition to the optical benefits of the mouse eye, the use of anesthesia reduces eye motion and pupil decentration, which can reduce the quality of human high-resolution retinal images. The advantages of the mouse for these experiments notwithstanding, the qualitative effects observed here in the mouse should accrue in the human eye, though the benefit of displacing the detector is expected to be smaller due to the larger axial PSF in the human retina (67 µm for a 6 mm pupil [17]).

Photoreceptor somas and red blood cells have a polarity expected of a positive lens. In blood cells, this is consistent with the higher index of refraction inside a red blood cell relative to plasma [20]. However, despite identical experimental conditions, we find that remarkably, horizontal cells have the polarity of a negative lens (Fig. 4). The signal polarity is dictated by the index of refraction inside/outside the cell and the convex or concave nature of their geometry.

Spatial variation in refractive index is apparently the origin the asymmetries characteristic of split detection and offset aperture images in ophthalmoscopy. This model implies that these approaches are ways to perform phase imaging in the living eye, and the mechanism to generate contrast is analogous to Schlieren imaging, oblique illumination, or differential phase contrast [21–23], where optical pathlength changes across the plane of focus deviate light in different directions.

Future work may build upon this model to design a detection mask that combines an optimized pattern, size, and lateral and axial offset to image specific cell types optimally in the retina. For example, the model predicts that the contrast of cells more vitread from the backscattering layer should benefit from larger lateral offsets than cells closer to the layer. Sapoznik *et al.* [24] have developed a detection mask that can be easily reconfigured and that could provide a convenient method for optimizing the detector configuration for each cell class, guided by the predictions of the wave optics model. While we have modeled the contrast benefit for the mouse in this study, the model also provides a prediction of improvement in the human eye, which has a lower NA (0.18). With equivalent parameters and adjusted NA, the model predicts a 1.7× improvement for translucent human cells.

REFERENCES

1. T. Y. P. Chui, D. A. VanNasdale, and S. A. Burns, Biomed. Opt. Express **3**, 2537 (2012).
2. D. Scoles, Y. N. Sulai, C. S. Langlo, G. A. Fishman, C. A. Curcio, J. Carroll, and A. Dubra, Invest. Ophthalmol. Vis. Sci. **55**, 4244 (2014).
3. A. Guevara-Torres, D. R. Williams, and J. B. Schallek, Biomed. Opt. Express **6**, 2106 (2015).
4. A. Guevara-Torres, A. Joseph, and J. B. Schallek, Biomed. Opt. Express **7**, 4228 (2016).
5. E. A. Rossi, C. E. Granger, R. Sharma, Q. Yang, K. Saito, C. Schwarz, S. Walters, K. Nozato, J. Zhang, T. Kawakami, W. Fischer, L. R. Latchney, J. J. Hunter, M. M. Chung, and D. R. Williams, Proc. Natl. Acad. Sci. USA **114**, 586 (2017).
6. A. Elsner, M. Miura, S. Burns, E. Beausencourt, C. Kunze, L. Kelley, J. Walker, G. Wing, P. Raskauskas, D. Fletcher, Q. Zhou, and A. Dreher, Opt. Express **7**, 95 (2000).
7. Y. N. Sulai, D. Scoles, Z. Harvey, and A. Dubra, J. Opt. Soc. Am. A **31**, 569 (2014).
8. M. Nomarski, J. Phys. Rad. **16**, S9 (1955).
9. Y. Geng, A. Dubra, L. Yin, W. H. Merigan, R. Sharma, R. T. Libby, and D. R. Williams, Biomed. Opt. Express **3**, 715 (2012).
10. G. Feng, R. H. Mellor, M. Bernstein, C. Keller-Peck, Q. T. Nguyen, M. Wallace, J. M. Nerbonne, J. W. Lichtman, and J. R. Sanes, Neuron **28**, 41 (2000).
11. I. Solovei, M. Kreysing, C. Lanctôt, S. Kösem, L. Peichl, T. Cremer, J. Guck, and B. Joffe, Cell **137**, 356 (2009).
12. J. W. Goodman, *Introduction to Fourier Optics* (Roberts & Company, 2005).
13. Y. Geng, L. A. Schery, R. Sharma, A. Dubra, K. Ahmad, R. T. Libby, and D. R. Williams, Biomed. Opt. Express **2**, 717 (2011).
14. R. H. Webb, G. W. Hughes, and F. C. Delori, Appl. Opt. **26**, 1492 (1987).
15. G. J. Van Blokland and D. Van Norren, Vis. Res. **26**, 485 (1986).
16. A. Dubra and Z. Harvey, *Biomedical Image Registration* (Springer, 2010), p. 60.
17. M. Born and E. Wolf, *Principles of Optics* (Cambridge University, 2002), p. 177, 491.
18. K. H. Kim, M. Puoris'haag, G. N. Maguluri, Y. Umino, K. Cusato, R. B. Barlow, and J. F. de Boer, J. Vis. **8**(1): 17 (2008).
19. R. A. Cuthbertson and T. E. Mandel, Invest. Ophthalmol. Vis. Sci. **27**, 1659 (1986).
20. A. G. Borovoi, E. I. Naats, and U. G. Oppel, J. Biomed. Opt. **3**, 364 (1998).
21. T. N. Ford, K. K. Chu, and J. Mertz, Nat. Methods **9**, 1195 (2012).
22. L. Joannes, F. Dubois, and J.-C. Legros, Appl. Opt. **42**, 5046 (2003).
23. D. K. Hamilton and C. J. R. Sheppard, J. Microsc. **133**, 27 (1984).
24. K. A. Sapoznik, T. Luo, A. de Castro, L. Sawides, R. L. Warner, and S. A. Burns, Biomed. Opt. Express **9**, 1323 (2018).